ELSEVIER

Sensible and latent heat flux in the tropical Pacific from satellite multi-sensor data

Young-Heon Jo[a], Xiao-Hai Yan[a],[*],[1], Jiayi Pan[a], W. Timothy Liu[b], Ming-Xia He[c]

[a] *Graduate College of Marine Studies, University of Delaware, 209 Robinson Hall, South College Avenue, Newark, DE 19716, USA*
[b] *Jet Propulsion Laboratory, California Institute of Technology, Pasadena, CA 91109, USA*
[c] *Ocean Remote Sensing Institute, Ocean University of Qingdao, China*

Abstract

Satellite multi-sensor data is used to derive sensible heat flux (SHF), Bowen ratio (Bo), and thus latent heat flux (LHF) in the tropical Pacific. The temperature differences at the air–sea interface are determined empirically for regions where strong deep air convection is present due to the buoyancy force. The vertical airflow results in surface wind divergence, which is estimated from scatterometer wind vector fields. The areas of positive temperature differences between sea surface temperature and atmospheric temperature estimated using surface wind divergence and in situ measurements are highly consistent in the tropical Pacific, especially in two convergence zones, i.e., the Intertropical Convergence Zone (ITCZ), and the South Pacific Convergence Zone (SPCZ). The bulk formulated SHF, determined by surface wind divergence (SHF_{BWD}), is compared with a long-term time series (January 1993–December 1999) of the SHF from the National Centers for Environmental Prediction (NCEP) reanalyzed model data (SHF_M). In the ITCZ, the correlation coefficients and the Root Mean Square (RMS) differences between SHF_{BWD} and SHF_M are over 70% and in the order of less than 4 W/m^2, respectively. Furthermore, the bulk formulated latent heat flux (LHF_B) is obtained using the empirical Bowen ratio (Bo_E) and SHF_{BWD}. The Bo_E for the tropical Pacific was estimated using only sea surface temperature, which is valid when the vapor is saturated near sea surface. The RMS differences between SHF_{BWD} and LHF_B are estimated as 3.5 and 39.3 W/m^2, respectively. In addition, the differences of SHF_{BWD} and LHF_B during the boreal winters are smaller than that in the boreal summers. Finally, in order to study spatial and temporal variations, we apply Empirical Orthogonal Function (EOF) analysis to SHF_{BWD} and LHF_B and compare with EOF analysis of Coupled Ocean and Atmosphere Data Set (COADS)'s SHF and LHF.
© 2004 Elsevier Inc. All rights reserved.

Keywords: Heat flux; Sensible heat flux; Latent heat flux; Bowen ratio; Wind divergence

1. Introduction

Throughout the world's oceans, a significant transfer of heat and vapor occurs at the air–sea interface, which then drive oceanic processes such as the redistribution of heat and vapor. Estimating the sensible heat flux (SHF) and the latent heat flux (LHF) is essential for understanding the physical mechanism of the air–sea interaction and has various applications including seasonal forecasting and climate predictions. However, because of the difficulties involved measuring SHF and LHF, very few direct methods are available. The eddy correlation or dissipation methods are the most accurate, but remain very sparse and, in most cases, cover only a narrow domain of the whole spectrum of atmospheric and oceanic conditions.

The bulk formulae are more commonly used to estimate turbulent surface heat fluxes on a global scale. As demonstrated in several studies, there are significant errors involved (Blanc, 1987; Planton et al., 1991; Wear, 1989), as well as large inherent errors (Blanc, 1985). The input variables of the bulk formulated SHF and LHF (wind speed, air temperature, humidity, and sea surface temperature) themselves suffer from measurement errors that can dramatically affect the accuracy of the estimated fluxes. As an example, Wear (1989) showed that the overall uncertainty on individual bulk-derived estimates of LHF can be

as large as 80 W/m^2. Because of systematic errors, estimations of the heat fluxes over a large number of observations still have an uncertainty exceeding 30 W/m^2. The LHF, as opposed to the sensible heat flux, was found to be a more problematic aspect of the study, as indicated by Bryan (1989). The total uncertainties due to systematic and random errors for individual observations of the net solar, infrared irradiances, the latent heat fluxes, and the sensible heat fluxes, using marine weather reports, were about 80, 10, 83, and 12 W/m^2, respectively.

Before the advent of satellite technology, the surface fluxes, especially SHF and LHF, had to be calculated exclusively relying on in situ measurements. Several important heat or vapor or both flux studies are based on in situ measurements and have addressed the upper-ocean heat budget in the equatorial Pacific (e.g., Bryden & Brady, 1989; Enfield, 1986; Hayes et al., 1991; Kessler & McPhaden, 1995; Stevenson & Niiler, 1983; Swenson & Hansen, 1999; Wyrtki, 1981). However, with satellite technology, we now have a complementary way to remotely derive surface fluxes with uniform spatial and temporal sampling. Unfortunately, these satellite observations also do have some critical problems. For instance, calculation of the SHF is dependent on air–sea temperature differences and is also limited by the rate at which heat can be transferred to the air–sea interface by processes within the atmospheric boundary layer. The estimation of air temperature is not directly accessible from remote sensing measurements. Thus many studies using satellite multi-sensor data are relying on the empirical formulae. Recently, Bentamy et al. (2003) estimated latent heat flux over the global oceans. Comparisons were made with not only in situ observations from buoys and ships, but also with the European Centre for Medium-Range Weather Forecasts (ECMWF) and the National Centers for Environmental Prediction (NCEP)–the National Center for Atmospheric Research (NCEP–NCAR) reanalyses data.

In order to estimate LHF, one can use SHF and Bowen ratio (LHF = SHF/Bo$_E$). Jo et al. (2002) showed that heat and moisture variations can be studied using the empirical Bowen ratio (Bo$_E$) in the tropical Pacific. As long as vapor on the sea surface is saturated, the Bo$_E$ can be independently estimated from sea surface temperature observations. However, most of the sea surface is not saturated with water vapor, so that the Bo$_E$ has to be corrected for the effects of the lower level of humidity and various ranges of wind. Compensating for unsaturated vapor on the sea surface, the Bo$_E$ provides significant advantages over the bulk formulated Bowen ratio (Bo$_B$ = SHF$_B$/LHF$_B$). Instead of estimating each SHF$_B$ (which is a function of temperature differences at the air–sea interface, wind, and parameters) and LHF$_B$ (which is a function of humidity differences at the air–sea interface, wind, and parameters) to obtain the Bo$_B$, Bo$_E$ is only a function of sea surface temperature. It

follows that the LHF can be estimated from the SHF if the Bowen ratio is known. In this study, the bulk formulated SHF, derived from the surface wind divergence (SHF$_{BWD}$) and the Bo$_E$, enables us to estimate the bulk formulated latent heat flux.

The purpose of the study is to describe the new method of computing SHF$_{BWD}$, which was first suggested by Pan et al. (2003) and which we modified in this study. The LHF is obtained by computing SHF$_{BWD}$/Bo$_E$. The details of the method for estimating the SHF are introduced in Section 2, and the data used in the study are described in Section 3. Our results are in Section 4. The correlations and Root Mean Square (RMS) differences between SHF$_{BWD}$ and the SHF obtained from the National Centers for Environmental Prediction (NCEP) reanalyzed model data (SHF$_M$) are computed. As means of comparison, long-term time series of two SHFs are generated for several oceanic regions after correcting the SHF$_{BWD}$ (Section 4.1). In order to study spatial and temporal variations of the sensible heat flux, the result of an Empirical Orthogonal Function (EOF) analysis are discussed in Section 4.2. The empirical Bowen ratio, determined using linear regression with NCEP reanalyzed model data, is presented in Section 4.3. The statistical and EOF analysis in Sections 4.1 and 4.2 for the SHF are also applied to the LHF in Sections 4.4 and 4.5, respectively. Conclusions follow in Section 5.

2. Methodology

Pan et al. (2003) developed a new method to estimate sensible heat flux on the basis of wind vector data. In this study, we made some modifications to this method, which are introduced as follows. Laboratory experiments have shown that the pressure, volume, and temperature of any material can be related by an equation of state. The ideal gas equation may be written as,

$$PV = mRT \tag{1}$$

where P, V, m, and T are the pressure, volume, mass, and temperature of the gas, respectively. R is a constant for 1 kg of a gas, and depends on the particular gas under consideration. Since $m/V = \rho_a$, where ρ_a is the air density, the ideal gas equation may also be written in the form

$$P = R\rho_a T \tag{2}$$

Air density can be a function of the vapor pressure (P_v) and the dry air pressure (P)

$$\rho_a = \frac{P - P_v}{R_d T} + \frac{P_v}{R_v T} \tag{3}$$

where R_d ($=287$ J/deg kg) and R_v ($=461$ J/deg kg) are the gas constants for 1 kg of dry air and 1 kg of water vapor, respectively.

Now, we consider that the buoyancy force resulting from the density differences of Eq. (3) due to temperature change is

$$\Delta F_b = g\Delta\rho V = -g\left[\left(\frac{P-P_v}{R_d}\right)\frac{1}{T^2}\Delta T + \frac{P_v}{R_v}\frac{1}{T^2}\Delta T\right]V \tag{4}$$

The upward buoyancy force of the rising air mass in a unit volume is equal to the downward gravitational force, i.e.,

$$\Delta F_b = \rho_v\frac{dw}{dt} = -g\left[\left(\frac{P-P_v}{R_d}\right)\frac{1}{T^2}\Delta T + \frac{P_v}{R_v}\frac{1}{T^2}\Delta T\right] \tag{5}$$

The rising water vapor is assumed to be saturated. Therefore, $\rho_v = \rho_{vs}$, and by taking the derivative with respect to the vertical direction (z) of Eq. (5), we obtain the following empirical temperature differences (ΔT_E) after having determined dz/dt empirically.

$$\Delta T_E = -\frac{dw}{dz}\frac{\rho_{vs}}{g}\frac{dz}{dt}\left[\left(\frac{P-P_v}{R_d}\right)\frac{1}{T^2} + \frac{P_v}{R_v}\frac{1}{T^2}\right]^{-1} \tag{6}$$

Finally, from the point of view of the wind field, the convergence zone is associated with a deep convection of airflow, which can be quantified by the ocean surface wind divergence defined as $(du/dx)+(dv/dy)$. By the continuity equation, we have

$$-\frac{dw}{dz} = \left(\frac{du}{dx} + \frac{dv}{dy}\right). \tag{7}$$

The conventional bulk formulated sensible heat flux is defined by

$$\text{SHF}_B = \rho_a C_P C_H \Delta T\,|\,W\,|, \tag{8}$$

and the new bulk formulated SHF using surface wind divergence after replacing ΔT in Eq. (8) with ΔT_E in Eq. (6) yields

$$\text{SHF}_{BWD} = \rho_a C_P C_H \Delta T_E\,|\,W\,| \tag{9}$$

where

$$\Delta T_E = \text{div}(W)\frac{\rho_{vs}}{g}\frac{dz}{dt}\left[\left(\frac{P-P_v}{R_d}\right)\frac{1}{T^2} + \frac{P_v}{R_v}\frac{1}{T^2}\right]^{-1} \tag{10}$$

The following parameters (Andreas & Cash, 1996) are used for this study:

$$\rho_a(T_s, P) = 1.2923\left(\frac{T_k}{Y_k + T_s}\right)\left(\frac{P}{1013.25}\right)$$

$$\rho_{vs}(T_s, P, S) = \frac{100 M_w P_v(T_s, P)}{R(T_k + T_s)}f(S)$$

$M_w = 18.0160 \times 10^{-3}$ kg/mol^{-1},

$R = 8.31441$ J/mol^{-1} K^{-1}, and

$T_k = 273.15$ K

$f(S) = 1 - 0.000537S$

and by Buck (1981)

$$P_v = [1.0007 + (3.46 \times 10^{-6}P)]\exp\left[\frac{17.502 T_s}{240.97 + T_s}\right]$$

T_s is sea surface temperature, S is sea surface salinity, W is the wind vector, and C_p is heat capacity. The transfer coefficient of heat (C_H) under unstable conditions has been determined through fitting field measurements or solving flux-profile relations (Bradley et al., 1991; DeCosmo et al., 1996; Fairall et al., 1996; Large & Pond, 1982).

The fundamental concept underlying this study is that when the sea surface temperature is greater than the air temperature ($\Delta T > 0$), or when there is atmospheric deep convergence, the warmed air rises due to increased buoyancy. In order to apply the method of estimating ΔT_E for SHF$_{BWD}$, we compared the areas of positive temperature difference from the Coupled Ocean and Atmosphere Data Sets (COADS) to the empirical ΔT_E in Eq. (10). The mean ΔT from the COADS climatological data is shown in the upper panel of Fig. 1. One may expect strong upwelling and convection of airflow over the western boundary currents (e.g., the Gulf Stream), the West Pacific Warm Pool (WPWP), the Intertropical Convergence Zone (ITCZ), and the South Pacific Convergence Zone (SPCZ). The areas, which always exhibit positive ΔT's, estimated using surface wind divergence in Eq. (10) are shown in the lower panel of Fig. 1. By comparing in situ data in Fig. 1a–b, we can see where we can apply this method. Since the model is highly applicable to the tropical Pacific, we applied this method to this location in order to estimate the heat and vapor fluxes. In the tropical Pacific, there are two systems bordering the equator: the ITCZ in the Northern Hemisphere and the SPCZ in the Southern Hemisphere.

3. Data

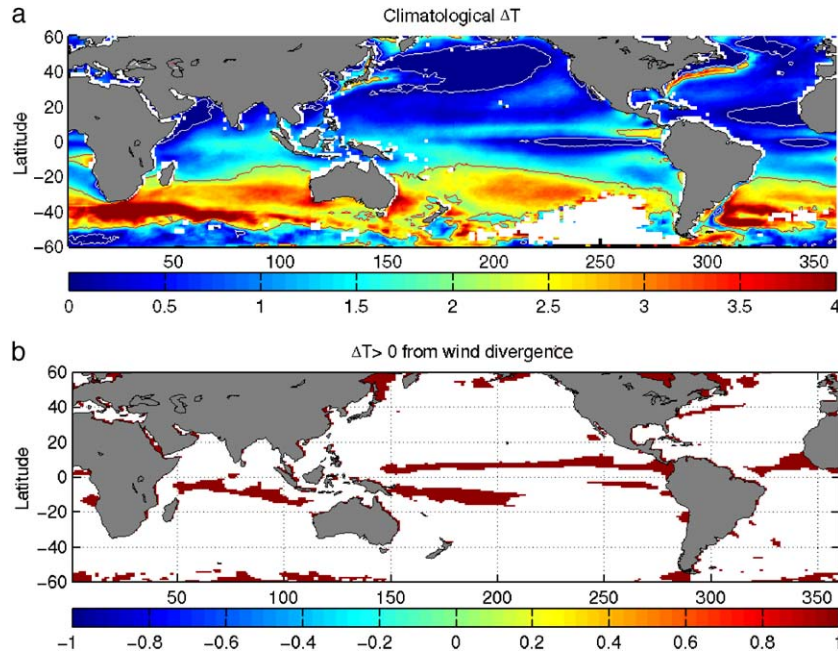The satellite wind data was derived from European Remote Sensing-1 (ERS-1), NASA Scatterometer (NSCAT),

Fig. 1. The upper panel shows the mean temperature differences (sea surface temperature – air temperature) in degrees using COADS. The areas of dark red in the lower panel shows the empirical temperature differences derived from Eq. (10), which is always positive.

and Quick Scatterometer (QuikSCAT) Active Microwave Instrument (AMI). The wind data of ERS-1/2 was obtained from the Institut Français de Recherche pour l'Exploitation de La Mer (IFREMER) at http://www.ifremer.fr/cersat/SERV-ICES/ARFTP/E_MWFIU.HTM. The NSCAT was launched aboard the Advanced Earth Observing Satellite (ADEOS) owned by the National Space Development Agency (NASDA)-Japan on August 6, 1996. Global daily data of NSCAT wind with a spatial resolution of 0.5 latitude by 0.5 longitude was obtained from the Jet Propulsion Laboratory (JPL). The RMS errors for wind speed and direction are approximately 2 ms^{-1} and 20°, respectively. The sea wind on QuikSCAT (June 1999–present) mission is a quick recovery to fill the gap created by the loss of data from the NSCAT. The NSCAT and the QuikSCAT wind data were obtained from the Physical Oceanography Distributed Active Archive Center (PODAAC) at http://podaac.jpl.nasa.gov/.

Global monthly mean Optimum Interpolated Sea Surface Temperature (OISST), with a spatial resolution of a 1° grid, from January 1993 to December 1999, was obtained from the National Oceanic and Atmospheric Administration/National Centers for Environmental Prediction (NOAA/NCEP). The monthly optimum interpolation (OI) fields were derived by a linear interpolation of the weekly OI fields to daily fields and then averaging the daily values over a month (Reynolds & Smith, 1994). The sources of OISST are based on COADS and satellite observations. During the 1990s, in situ data was obtained from the Global Telecommunication System, and the satellite observations were obtained from operational data produced by the National Environmental Satellite Data and Information Service (NESDIS).

Global climatological fields of the monthly mean air–sea fluxes of heat are presented in the Max Planck Institute's Heat Fluxes (MPIHF) data sets. These data sets contain climatological monthly means of heat fluxes and radiation budgets over the global oceans, based on analyses of the COADS (Slutz et al., 1985) for the period of 1950–1979. All data are given on a 2° latitude/longitude grid. Meteorological and oceanographic parameters contained in these data sets include air temperature, relative humidity, wind speed, latent heat flux, sensible heat flux, etc.

Surface heat fluxes have been calculated from weather data using numerical weather models by various reanalysis. The fluxes are consistent with atmospheric dynamics, they are global, and they are available for many years on a uniform grid. One of the most well known global reanalysis comes from the NCEP and the NCAR (Kalnay et al., 1996). The SHF$_M$ and the LHF$_M$ were obtained from reanalyzed model data of the NOAA/NCEP.

4. Results

4.1. Correlation coefficients and RMS differences between SHF$_M$ and SHF$_B$

Using a monthly mean long-term time series from January 1993 to December 1999, correlation coefficients and RMS differences between SHF$_{BWD}$ and SHF$_M$ are given in Fig. 2. The SHF$_{BWD}$ was estimated using Eq. (9) using 1/15 ms^{-1} for dz/dt (empirically determined based in Fig. 3a) in the ΔT_E (Eq. 10) and multiplying the surface wind divergence by a factor of 10^5. Fig. 2 clearly shows

highly correlated areas and small RMS differences in the two convergence zones. The ITCZ is an east–west belt just north of the equator which migrates seasonally between 5 °N in March and April and approximately 12 °N latitude in August and September (Zheng et al., 1997). Meanwhile the SPCZ stretches southeastward across the southeastern tropical Pacific (Zheng et al., 1997). While the areas of the upwelling air mass ($\Delta T > 0$) in the ITCZ and the SPCZ show highly positive correlations, the area of downwelling air mass ($\Delta T < 0$) off the coast of Peru shows highly negative correlations. The contours in Fig. 2a and b are the mean SHF in W/m^2 derived from the COADS to help interpretation of this method with the correlations and the RMS differences. The high correlations are on the high COADS's mean SHF ($O(6-8$ W/m^2)) in the ITCZ and the SPCZ, which support the applicable areas of this method (Fig. 2a). For the quantitative comparison, Fig. 2b shows how much the RMS differences differ from the mean SHF (Fig. 2b). The low RMS differences ($O(1-2$ W/m^2)) are on the high COADS's mean SHF ($O(6-8$ W/m^2)).

Six adjacent areas in the ITCZ were selected to compare the long-term time series of the SHF$_M$ and the SHF$_{BWD}$. Fig. 3a shows the linear relationship between the SHF$_M$ and the SHF$_{BWD}$. The diagonal line indicates the slope as 1, obtained after subtracting 3 W/m^2 from the original SHF$_{BWD}$ thus obtaining the best fit. The RMS difference between the two SHFs is 3.51 W/m^2 for this case. For further comparison, the long-term time series of the SHF$_M$ (dashed line) and the

SHF$_{BWD}$ (solid line) were shown in Fig. 3b. The correlations and the RMS are within 66–73% and 2.7 W/m^2, respectively. The RMS differences are smaller during boreal winters and springs than during boreal summers and falls.

4.2. Spatial and temporal variations for the SHF using EOFs

For spatial and temporal variation, EOF is widely used to decompose a long-term time series of spatially observed data set into orthogonal spatial and temporal modes. EOF and amplitudes can be calculated in a single step using singular value decomposition (SVD) without constructing either version of the covariance matrix as shown by Kelly (1988). In practical terms, EOFs are a means of reducing the size of a data set while retaining a large fraction of the variability present in the original data. The temporal variance of the data is partitioned into orthogonal spatial patterns, which are the eigenvectors of the covariance matrix. Each eigenvector has a long-term time series of coefficients associated with it that represent the modulation of the importance of the particular eigenvector as a function of time. The time series is most often normalized to unit variance with the total variance of the time series carried by the eigenvalue.

EOF analysis was applied to the SHF$_{BWD}$ and shown in Fig. 4a for the first and the second spatial and temporal EOFs with a variance of 32%, and 22%, respectively. The first spatial EOF shows the Northern and Southern Hemi-
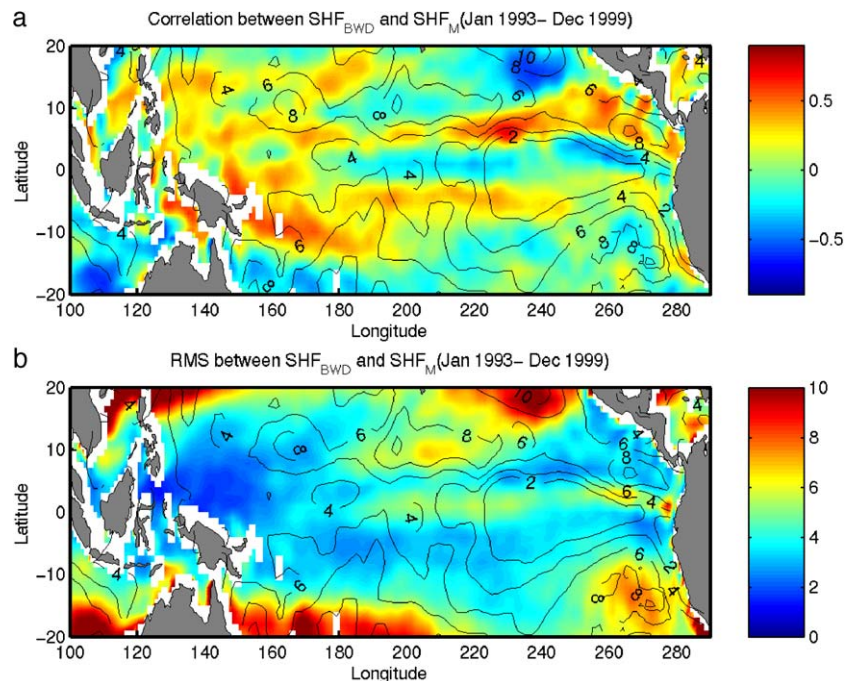

Fig. 2. Correlation coefficients and RMS differences between the bulk formulated sensible heat flux using surface wind divergence (SHF$_{BWD}$) and the sensible heat flux from the NCEP reanalyzed model data (SHF$_M$) using long-term time series (January 1993–December 1999). The contour lines represent mean COADS' SHF in W/m^2.
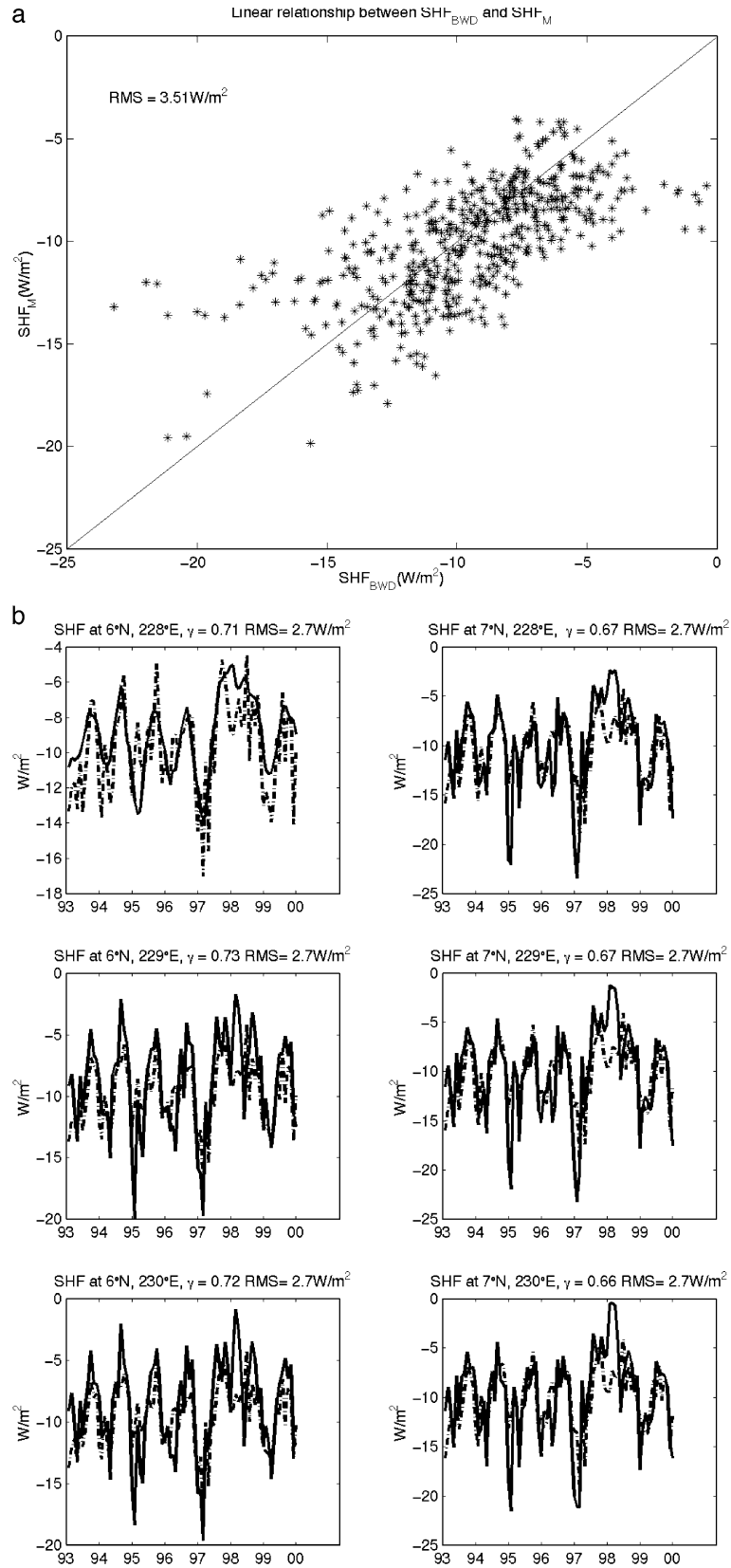
Fig. 3. (a) Linear relationship between SHF_{BWD} and SHF_M data. The data were selected in the ITCZ from January 1993 to December 1999. The RMS difference between two SHFs is 3.51 W/m². (b) Long-term time series of the SHF_{BWD} and the SHF_M at given areas (January 1993–December 1999). The SHF_M are shown with a dashed line, and the SHF_{BWD} are shown with a solid line. The differences are smaller during boreal winters and springs than that during boreal summers and fall.

sphere annual variations with the local maxima in March
and the local minima in September, except during 97–98
(local maxima in January 1998) El Niño event where an
interannual signal is evident. The second spatial EOF is
similar to the first spatial EOF, but with the local maxima
occurring in July and the local minima in January, except
in 1997–1998.

Fig. 4b shows the first and the second spatial and
temporal EOFs of SHF derived from the COADS with a
variance of 67% and 29%, respectively. The first spatial
EOFs show strong coastal upwelling in the eastern tropical
Pacific, which is similar to the first spatial EOFs in Fig. 4a
with the local maxima in January and the local minima in
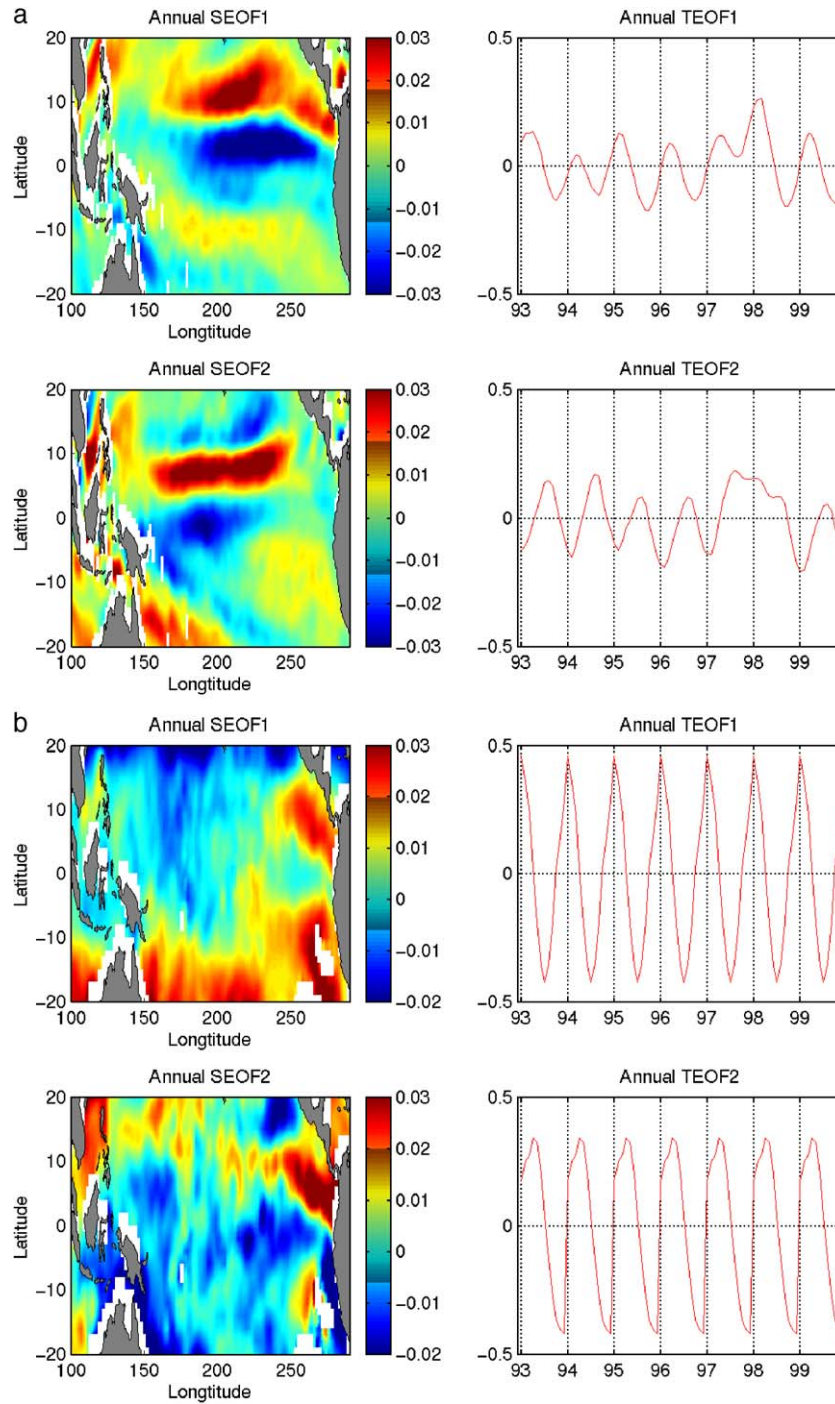June. The second spatial EOFs are similar to the second

Fig. 4. (a) The first and the second spatial and temporal EOFs for the annual SHF$_{BWD}$. The variance of the first and the second mode is 32% and 22%, respectively. (b) The first and the second spatial and temporal EOFs for the SHF from the COADS. The variance of the first and the second mode is 67% and 29%, respectively.
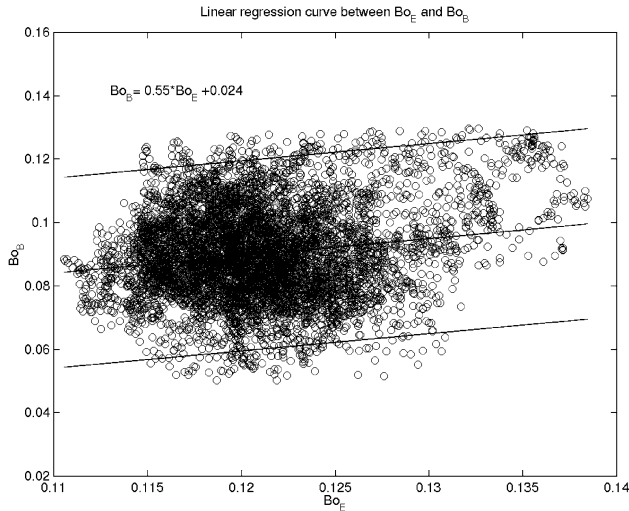
Fig. 5. Linear regression curve between empirical Bowen ratio (Bo_E) using sea surface temperature and the bulk formulated Bowen ratio ($Bo_B = SHF_M/LHF_M$) using NCEP reanalyzed model data.

spatial EOFs in Fig. 4b with the local maxima in April and the local minima in November. Because the method of SHF_{BWD} is more applicable in the tropical Pacific (especially for the ITCZ and the SPCZ), the spatial features of the two SHFs are similar at those latitudes, especially in the eastern tropical Pacific. The temporal SHF_{BWD} shows the 97–98 El Niño event signal, whereas the temporal EOFs for the SHF does not. The lack of an El Niño signal is due to the fact that the SHF is derived from COADS data, which is a climatology.

4.3. Determination of the Bowen ratio

The empirical equilibrium Bowen ratio is obtained by Andreas and Cash (1996), i.e.,

$$Bo^*(T_s, P, S) = \frac{\rho(T_s, P)C_P(T_s)}{L_v(T_s)\rho_{vs}(T_s, P, S)}$$
$$\times \left[\frac{ab}{(b+T_s)^2} - \frac{1}{(T_k + T_s)} \right]^{-1} \quad (11)$$

where $a = 17.502$ and $b = 240.97$ °C for $T_s > 0$ °C. The other parameters ($\rho(T_s,P)$, $C_p(T_s)$, $L_v(T_s)$, $\rho_{vs}(T_s,P,S)$) were already well defined in Section 2. The empirical Bowen ratio in the tropical Pacific has been studied by Jo et al. (2002). We compensated the wind and humidity effects on the unsaturated vapor on the sea surface for Bo_E using the COADS. Then, the Bo_B was computed using 7 years of the SHF_M and the LHF_M, and the Bo_E was estimated (Fig. 5) using OISST. The best regression curve determined was $Bo_E = 0.55 \times Bo^* + 0.024$. The upper and lower solid lines show the upper and lower bound for the Bo_B by a factor of ± 0.03.

4.4. Correlation coefficients and RMS between LHF_M and LHF_B

To estimate the bulk formulated latent heat flux (LHF_B), we used the SHF_{BWD} and the Bo_E; $LHF_B = SHF_{BWD}/Bo_E$. In
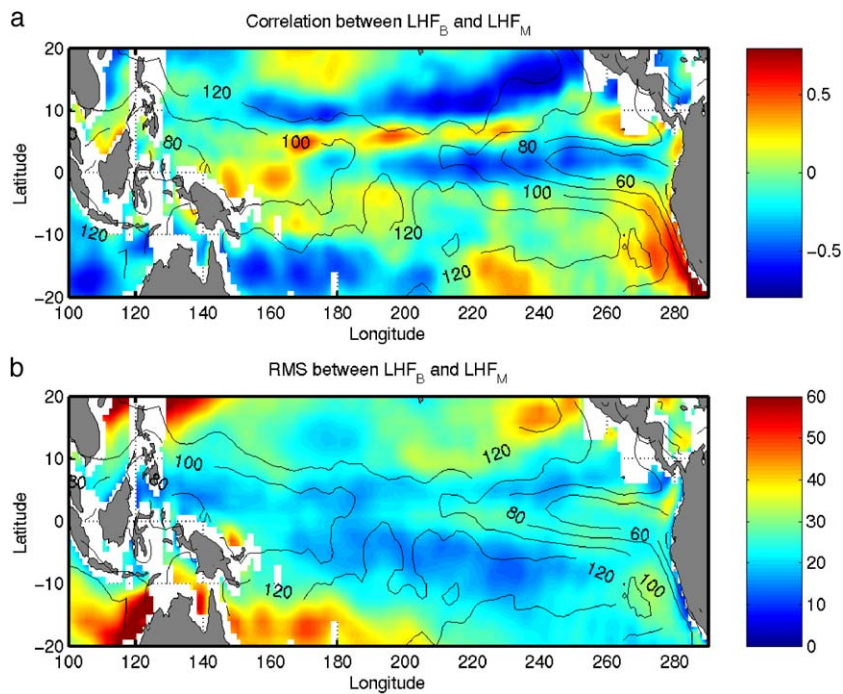

Fig. 6. Correlation coefficients and RMS differences between LHF_{BWD} ($= SHF_{BWD}/Bo_E$) and LHF_M using long-term time series (January 1993–December 1999).
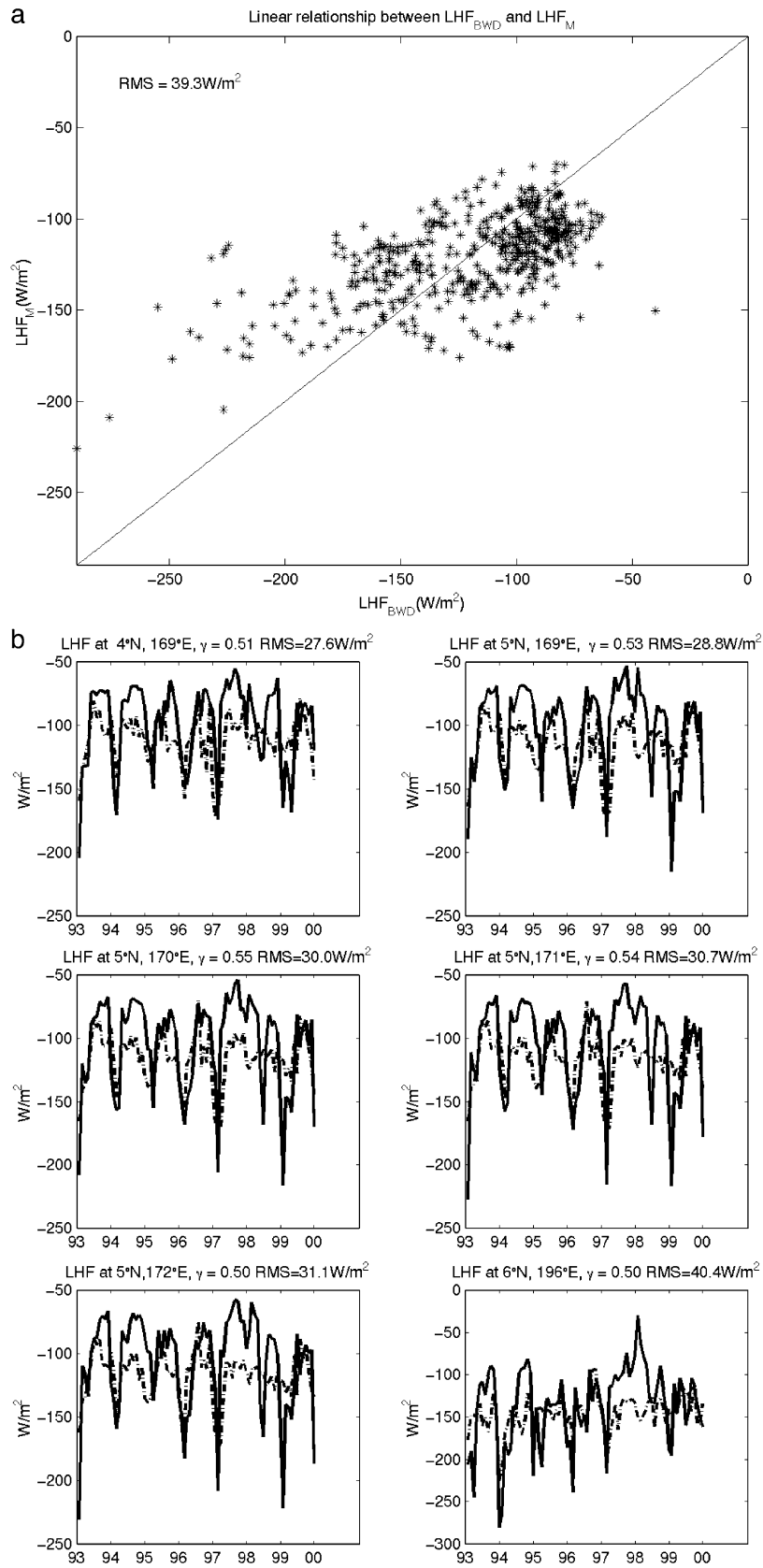
Fig. 7. (a) Linear relationship between LHF_B and LHF_M data. The data were selected in the ITCZ from January 1993 to December 1999. The RMS difference between two LHFs is 39.3 W/m². (b) Long-term time series of the LHF_B and the LHF_M at given areas (January 1993 – December 1999). The LHF_M are shown with a dashed line and the LHF_B are shown with a solid line. The differences are smaller during boreal winters and springs than that during boreal summers and fall.

order to estimate the discrepancy between LHF_M and LHF_B, we computed correlation coefficients and RMS differences, as shown in Fig. 6, using a long-term time series (January 1993–December 1999). The LHF_M were obtained from the NCEP reanalyzed model data. We can see highly correlated areas and small RMS in the tropical Pacific, especially in the ITCZ and the SPCZ. While the areas of the upwelling air mass due to the positive ΔT show highly positive correla-

tions, the area of a downwelling air mass off the coast of Peru shows highly negative correlations. The contours in Fig. 6a and b are the mean LHF in W/m^2 derived from the COADS to help the interpretation of the method with the correlations and the RMS differences (Fig. 6a). The high correlations are on the high COADS's mean high LHF ($O(100–120 \ W/m^2)$) in the ITCZ and the SPCZ, which support the applicable areas of the method. For the quanti-
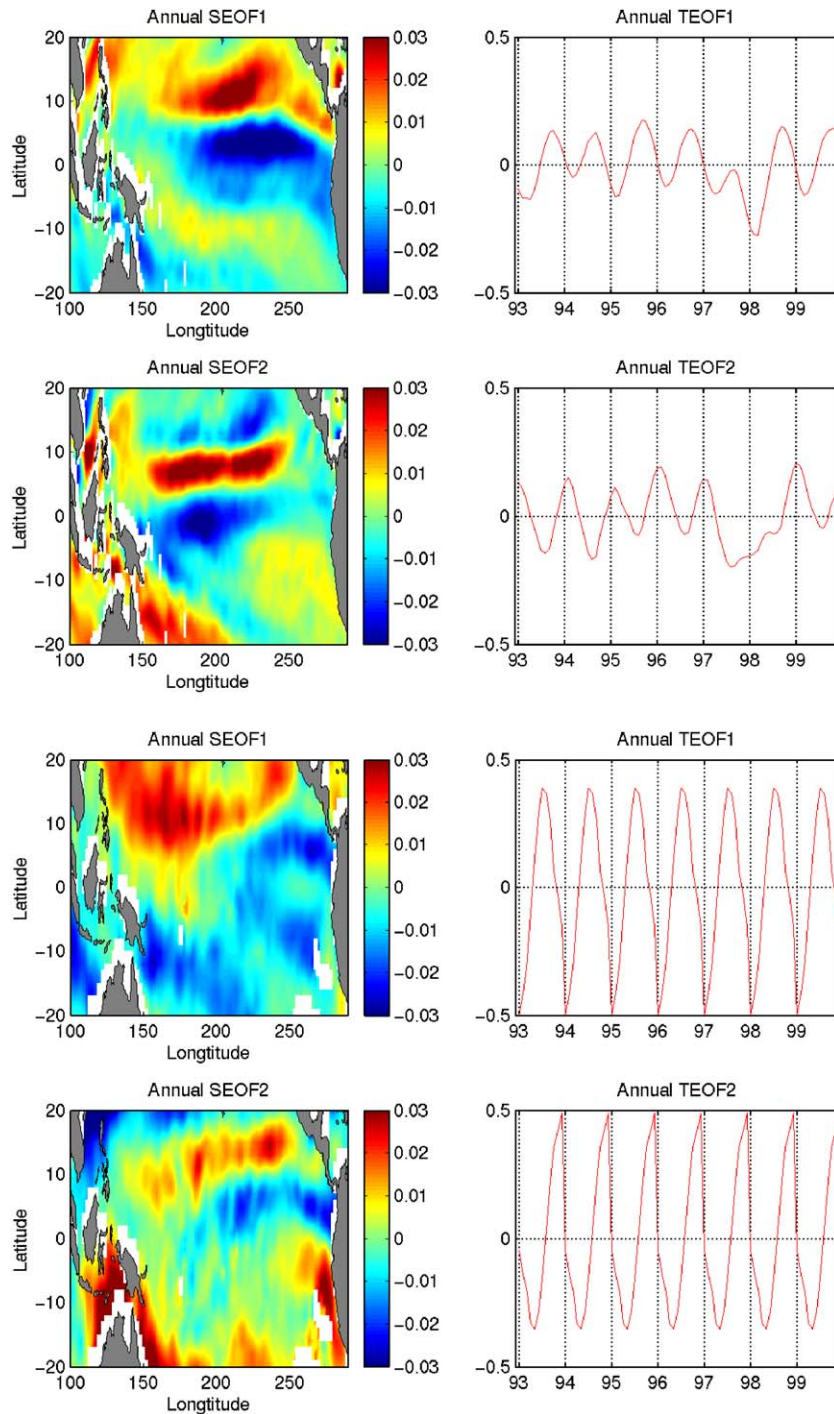

Fig. 8. (a) The first and the second spatial and temporal EOFs for the annual LHF_B. The variance of the first and the second mode is 35% and 21%, respectively. (b) The first and the second spatial and temporal EOFs for the COADS's LHF. The variance of the first and the second mode is 65% and 31%, respectively.

tative comparison, Fig. 6b shows how much the RMS differences differ from the mean LHF (Fig. 6b). The low RMS differences ($O(10-25$ W/m^2)) are on the high COADS's mean LHF ($O(100-120$ W/m^2)).

Six adjacent areas were selected to compare the long-term time series of the LHF$_M$ and the LHF$_{BWD}$. Fig. 7a shows the linear relationship between the LHF$_M$ and the LHF$_{BWD}$. The diagonal line indicates the slope as being 1, which was obtained after subtracting 70 W/m^2 from the LHF$_{BWD}$ for best fit. The RMS difference between the two LHFs is 39.3 W/m^2. For further comparison, the long-term time series of the LHF$_M$ (dashed line) and the LHF$_{BWD}$ (solid line) are shown in Fig. 7b. The correlations and the RMS are within $50-55\%$ and $27.6-40.4$ W/m^2, respectively. The RMS differences are smaller during boreal winters and springs than that during boreal summers and falls.

4.5. Spatial and temporal variations for the LHF using EOFs

EOF analysis is applied to LHF$_B$. Fig. 8a shows the first and the second spatial and temporal EOFs with a variance of 35% and 21%, respectively. The first spatial EOF shows Northern and Southern Hemisphere annual variations with local maxima in July and local minima in February, except during 97–98 El Niño event where an interannual signal is evident. The second spatial EOF shows the eastern and the western variations with local maxima in January and local minima in July rather than all Northern and Southern Hemisphere variations.

Fig. 8b shows the first and the second spatial and temporal EOFs of the LHF derived from COADS with a variance of 65% and 31%, respectively. The first spatial EOF shows Northern and Southern Hemisphere variations with local maxima in June and local minima in December. The second spatial EOF depicts the first EOF in more detail with local maxima in November and local minima in April. Each spatial EOF in Fig. 8a and b is similar, especially the second spatial mode. The first and the second spatial EOF in the tropical Pacific appear to be related by a 180° phase shift.

5. Conclusions

Thanks to satellites' excellent spatial and temporal coverage, the satellite data sets with a new method are potentially useful in studying heat and vapor flux through the air–sea interface. Throughout this study, we presented a new method of obtaining the SHF and the LHF based on the bulk formulae. Although this method is only applicable where there are strong convergence zones, it will contribute to the study of the ITCZ and the SPCZ in terms of SHF and LHF using scatterometer measurements. We found that the correlation coefficients and the RMS differences between the SHF$_{BWD}$ and the SHF$_M$ are over 70% and 3.5 W/m^2,

respectively. The Bo$_E$ for the tropical Pacific was estimated using only sea surface temperature after compensating unsaturated water vapor on the sea surface. Using 7 years of the SHF$_M$ and the LHF$_M$, the Bo$_B$ was computed, and using OISST, the Bo$_E$ was estimated. The best regression curve was determined as Bo$_E = 0.55 \times$ Bo* $+ 0.024$.

Finally, the bulk formulated latent heat flux (LHF$_B$) was obtained using the empirical Bowen ratio (Bo$_E$) and the SHF$_{BWD}$. The correlation coefficients and the RMS differences between the LHF$_{BWD}$ and LHF$_M$ are over 60% and 39.3 W/m^2, respectively. Compared to the uncertainties reported by others, this method provides better results with low RMS differences. The RMS differences between SHF$_{BWD}$ and LHF$_B$ were estimated to be 3.5 and 39.3 W/m^2, respectively. In addition, the RMS differences of SHF$_{BWD}$ and LHF$_B$ during boreal winters were smaller than that in boreal summers (Figs. 3b and 7b). Finally, in order to study spatial and temporal variations, we applied EOF analysis to SHF$_{BWD}$ and LHF$_B$ and compared that with EOF analysis of COADS's SHF and LHF. Each spatial EOF feature of SHF$_{BWD}$ (Fig. 4a) and SHF (Fig. 4b) is similar to the eastern tropical Pacific rather than the western tropical Pacific. The second spatial EOF feature of SHF$_{BWD}$ (Fig. 8a) and SHF (Fig. 8b) is similar to the first spatial EOF feature. The temporal EOFs of the SHF$_{BWD}$ and the LHF$_{BWD}$ determined from the long-term time series are more physically meaningful than the climatological SHF and LHF.

Today, advances in satellite technologies, better algorithms, and detailed sampling in time and space promise that sufficient measurements can be obtained in the near future enabling a better understanding of climate variability and predictability. Furthermore, global estimates of the heat flux at the sea surface (together with fluxes of momentum and sensible heat) could be very useful for verifying coupled ocean–atmosphere models, as well as driving ocean models.

References

Andreas, E. L., & Cash, B. A. (1996). A new formulation for the Bowen ratio over saturated surfaces. *Journal of Applied Meteorology*, *35*, 1279–1289.

Bentamy, A., Katsaros, K. B., Mestas-Nunez, A. M., Drennan, W. M., Forde, E. B., & Roquet, H. (2003). Satellite estimates of wind speed and latent heat flux over the global oceans. *Journal of Climate*, *15*, 637–656.

Blanc, T. V. (1985). Variation of bulk-derived surface flux, stability, and roughness results due to the use of different transfer coefficient schemes. *Journal of Physical Oceanography*, *15*, 650–669.

Blanc, T. V. (1987). Accuracy of bulk-method-determined flux, stability, and sea surface roughness. *Journal of Geophysical Research*, *92*, 3867–3876.

Bradley, E. F., Coppin, P. A., & Godfrey, J. S. (1991). Measurements of sensible and latent heat flux in the western equatorial Pacific Ocean. *Journal of Geophysical Research*, *96*, 3375–3389.

Bryan, C. W. (1989). Uncertainties in estimates of surface heat fluxes derived from marine reports over the tropical and subtropical oceans. *Tellus*, *41A*, 357–370.

Bryden, H. L., & Brady, E. C. (1989). Lateral mixing in the equatorial Pacific Ocean. *Journal of Marine Research*, *47*, 55–79.

Buck, A. L. (1981). New equations for computing vapor pressure and enhancement factor. *Journal of Applied Meteorology*, *20*, 1527–1532.

DeCosmo, J., Katsaros, K. B., Smith, S. D., Anderson, R. J., Oost, W. A., Bumke, K., & Chadwick, H. (1996). Air–sea exchange of water vapor and sensible heat: The humidity exchange over the sea (HEXOS) results. *Journal of Geophysical Research*, *101*, 12001–12016.

Enfield, D. B. (1986). Zonal and seasonal variations in the near-surface heat balance of the equatorial ocean. *Journal of Physical Oceanography*, *16*, 1038–1054.

Fairall, C. W., Bradley, E. F., Rogers, D. P., Edson, J. B., & Young, G. S. (1996). Bulk parameterization of air–sea fluxes for tropical ocean-global atmosphere coupled-ocean atmosphere response experiment. *Journal of Geophysical Research*, *101*, 3747–3764.

Hayes, S. P., Chang, P., & McPhaden, M. J. (1991). Variability of the sea surface temperature in the eastern equatorial Pacific during 1986–1988. *Journal of Geophysical Research*, *96*, 10553–10566.

Jo, Y. -H., Yan, X. -H., Pan, J., He, M. -X., & Liu, W. T. (2002). Calculation of the Bowen ratio in the tropical Pacific using sea surface temperature data. *Journal of Geophysical Research*, *107* (17-1–7-16).

Kalnay, E., et al. (1996). The NCEP/NCAR 40-year reanalysis project. *Bulletin of the American Meteorological Society*, *77*, 437–471.

Kelly, K. A. (1988). Comment on "Empirical orthogonal function analysis of advanced vary High Resolution Radiometer surface temperature patterns in Santa Barbara channel" by G.S.E. Lagerloef and R.L. Bernstein. *Journal of Geohysical Research*, *93*, 15753–15754.

Kessler, W. S., & McPhaden, M. J. (1995). The 1991–1993 El Nino in the Central Pacific. *Deep-Sea Research. Part 2. Topical Studies in Oceanography*, *42*, 295–334.

Large, W. G., & Pond, S. (1982). Sensible and latent heat flux measurements over the ocean. *Journal of Physical Oceanography*, *12*, 464–482.

Pan, J., Yan, X. -H., Jo, Y. -H., & Liu, W. T. (2003). A new method for estimation of the sensible heat flux in the unstable condition using satellite vector winds. *Journal of Physical Oceanography* (in press).

Planton, S., Deque, M., & Bellevaux, C. (1991). Validation of an annual cycle simulation with a T42-L20 GCM. *Climate Dynamics*, *5*, 189–200.

Reynolds, R. W., & Smith, T. M. (1994). Improved global sea surface temperature analyses using optimum interpolation. *Journal of Climate*, *7*, 929–948.

Slutz, R. J., Lubker, S. J., Hiscox, J. D., Woodruff, S. D., Jenne, R. L., Steurer, P. M., & Elms, J. D. (1985). *Comprehensive ocean–atmosphere data set; release 1*. Boulder, CO: Climate Research Program.

Stevenson, J. W., & Niiler, P. P. (1983). Upper ocean heat budge during the Hawaii-to-Tahiti Shuttle Experiment. *Journal of Physical Oceanography*, *13*, 1894–1907.

Swenson, M. S., & Hansen, D. V. (1999). Tropical Pacific Ocean mixed layer heat budge: The Pacific cold tongue. *Journal of Physical Oceanography*, *29*, 69–82.

Wear, B. C. (1989). Uncertainties in estimates of surface heat fluxes derived from marine reports over the tropical and subtropical oceans. *Tellus. Series A, Dynamic Meteorology and Oceanography*, *41*, 357–370.

Wyrtki, K. (1981). An estimate of equatorial upwelling in the Pacific. *Journal of Physical Oceanography*, *11*, 1205–1214.

Zheng, Q., Yan, X. -H., Liu, T., Tang, W., & Kurz, D. (1997). Seasonal and interannual variability of atmospheric convergence zones in the tropical Pacific observed with ERS-1 scatterometer. *Geophysical Research Letters*, *24*, 261–263.